Supporting Information

Transparent Amorphous Strontium Titanate Resistive Memories with Transient Photo-Response

*Taimur Ahmed, Sumeet Walia, Jeeson Kim, Hussein Nili, Rajesh Ramanathan, Edwin L. H. Mayes, Desmond W. M. Lau, Omid Kavehei, Vipul Bansal, Madhu Bhaskaran, and Sharath Sriram**

Taimur Ahmed, Sumeet Walia, Jeeson Kim, Hussein Nili, Omid Kavehei, Madhu Bhaskaran, Sharath Sriram
Functional Materials and Microsystems Research Group and Micro Nano Research Facility, RMIT University, Melbourne, VIC 3001, Australia
E-mail: taimur.ahmed@rmit.edu.au, sharath.sriram@rmit.edu.au
Hussein Nili
Present Address: Electrical and Computer Engineering Department, University of California Santa Barbara, Santa Barbara, CA 93106 (USA)
Rajesh Ramanathan, Vipul Bansal
Ian Potter NanoBioSensing Facility, NanoBiotechnology Research Laboratory, School of Science, RMIT University, Melbourne, VIC 3001, Australia
Edwin L. H. Mayes
RMIT Microscopy and Microanalysis Facility, RMIT University, Melbourne, VIC 3001, Australia
Desmond W. M. Lau
ARC Centre of Excellence for Nanoscale BioPhotonics & School of Science, RMIT University, Melbourne, VIC 3001, Australia

1. Area dependent resistive switching characteristics

In transition metal oxides, the bipolar resistive switching behaviour is usually attributed to the formation and rupture of localized filamentary pathways due to redox processes.[1, 2] Under a filamentary switching mechanism, the lateral dimensions of the memory cell are not expected to influence the resistive switching properties. Fig. S1 shows the correlation between HRS/LRS read currents and the area of our *t*-ReRAM cells. Unlike interfacial resistive switching, where the resistance–area product is independent of cell size,[3] our *t*-ReRAMs show an increase in the product with increasing cell size. This further indicates that the switching mechanism in both Device BL15 (Fig. S1a) and Device BL5 (Fig. S1b) is of a filamentary nature.

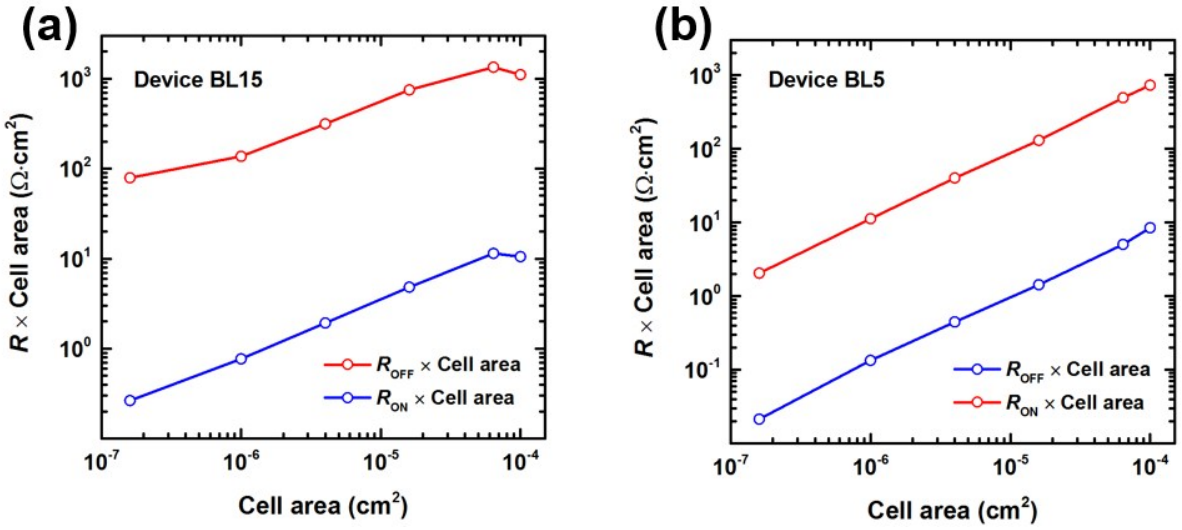

Fig. S1 The resistance–area product of Device BL15 (a) and Device BL5 (b) in HRS and LRS. The resistances are measured for varying cell sizes at a V_{READ} of 0.5 V.

2. Stoichiometric analysis of ITO thin films

The XPS analysis was carried out to characterize the composition and identify the chemical states of the principal elements in sputtered ITO (50 nm) thin films on glass. Curve-fitting of the core level spectra (O 1*s*, Sn 3$d_{5/2}$ and In 3$d_{5/2}$) for two types of ITO thin films, namely – as-grown and post-deposition annealed at 400 ˚C, is shown in Fig. S2.

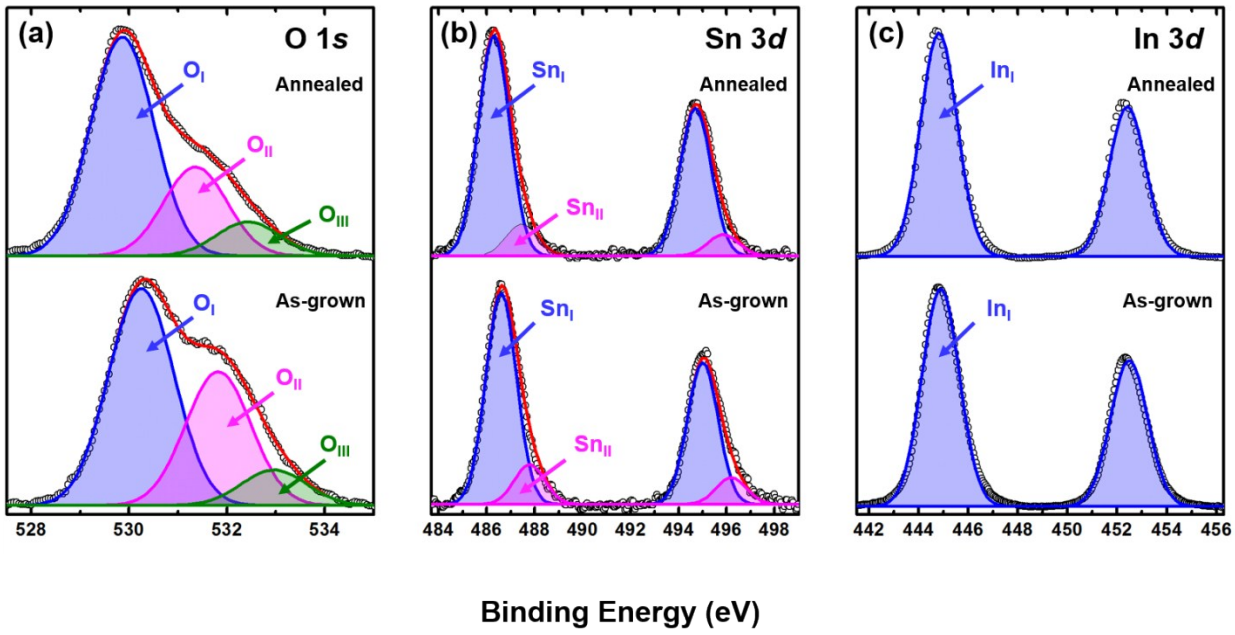

Fig. S2 High resolution XPS spectra corresponding to (a) O 1*s* (b) Sn 3*d* and (c) In 3*d* for the as-grown and post-deposition annealed ITO (50 nm) thin films.

The characteristic peaks positions are within the corresponding rage and are comparable to those reported in the literature.[4-7] All sub-peaks of principal elements have been labeled to distinguish among them and their positions are listed in Table S1. The O 1*s* spectra have been fitted with three peaks centered at 530.3 eV (O_I), 531.8 eV (O_{II}), 533.0 eV (O_{III}) for as-grown, and 529.9 eV (O_I), 531.4 eV (O_{II}) and 532.4 eV (O_{III}) for the post-deposition annealed sample. It is believed that the room temperature sputtering of ITO in a pure Ar environment results in oxygen deficient thin films, originating O_I and O_{II} peaks in the XPS spectra due to the formation of two types of O^{2-} ions.[5] Whereas O_{III} at higher binding energies (533.0 eV and 532.4 eV for as-grown and annealed samples, respectively) is associated with $In(OH)_x$ present on the surface.[4, 7] The presence of oxygen deficient regions such as oxygen vacancies (V_o) and Sn centers, in ITO thin film act as charge trapping sites, making In 3*d* peaks insensitive to the concentration V_o and Sn species.[7] In the literature, it is suggested that the O_{II}/O_I ratio can be used to estimate the oxygen

deficiency in the ITO thin films.[5] The calculated O_{II}/O_I ratios (listed in **Table S1**) for our sputtered ITO thin films show that as-grown ITO thin films are more oxygen deficient than the post-deposition annealed thin films.

Table S1. Peak positions of the resolved core level XPS spectra from the principal elements in as-grown and post-deposition annealed ITO thin films.

	Labels	Peak positions (eV)	
		As-grown	Annealed
O 1*s*	O_I	530.3	529.9
	O_{II}	531.8	531.4
	O_{III}	533.0	532.4
Sn 3*d*$_{5/2}$	Sn_I	486.9	486.3
	Sn_{II}	487.6	487.5
In 3*d*$_{5/2}$	In_I	444.9	444.8
	O_{II}/O_I	0.62	0.41

3. Optical transmission characterization of ITO thin films

Optical transmission characteristics of both as-grown and post-deposition annealed ITO thin films (50 nm), within the optical range of 300-800 nm, are shown in Fig. S3. The average transmission increased after post-deposition annealing at 400 ˚C in air which is consistent with the literature.[4]

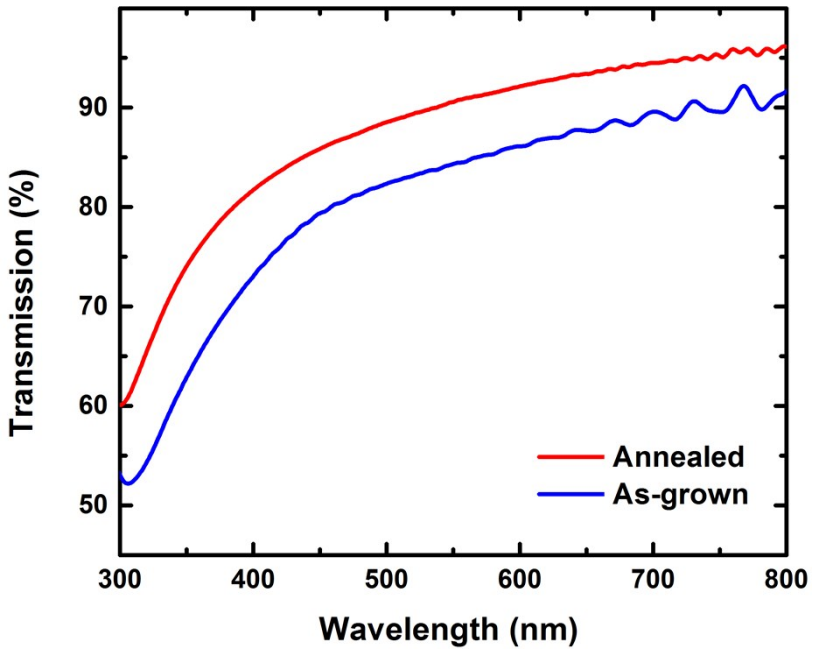

Fig. S3 Optical transmission characteristics of the ITO (~50 nm) thin films sputtered at room temperature on glass substrates.

4. Electrical characterization of single layer and bilayer *t*-ReRAM cells with symmetric interfaces

The *I–V* characteristics of a single layer (ITO/*a*-STO_x (35 nm)/ITO) and bilayer (ITO/*a*-STO_x (10 nm)/*a*-STO_y (15 nm)/ITO) are shown in Fig. S4a and Fig. S4b, respectively.

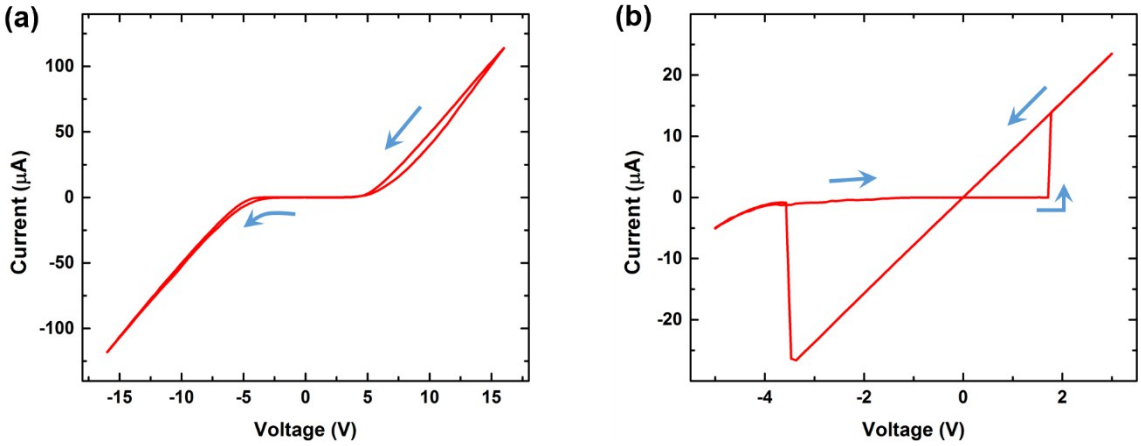

Fig. S4 Electrical characterization of transparent devices with symmetric interfaces. (a) *I–V* characteristics of single layer ITO/*a*-STO_x/ITO cell. (b) *I–V* characteristics of bilayer ITO/*a*-STO_x/STO_y/ITO cell.

5. Optical characterization

UV-Vis transmission and reflectance spectra of sputtered functional bilayer (*a*-STO_x/*a*-STO_y) oxide stack, bottom (ITO) and top (ITO/Ti) electrodes of our devices are shown in Fig. S5a and S5b, respectively. The bottom ITO electrodes are post-deposition annealed (at 400 ˚C in air) to improve the transparency of *t*-ReRAM cells, instead of annealing top ITO/Ti electrode which may permanently diffuse the interfaces at high temperature and deteriorate the resistive switching performance of the devices. Fig. S6 shows the reflectance spectra of both Device BL5

and Device BL15. The reflectance spectra are collected from device (ITO/Ti/*a*-STO_x/*a*-STO_y/ITO) region.

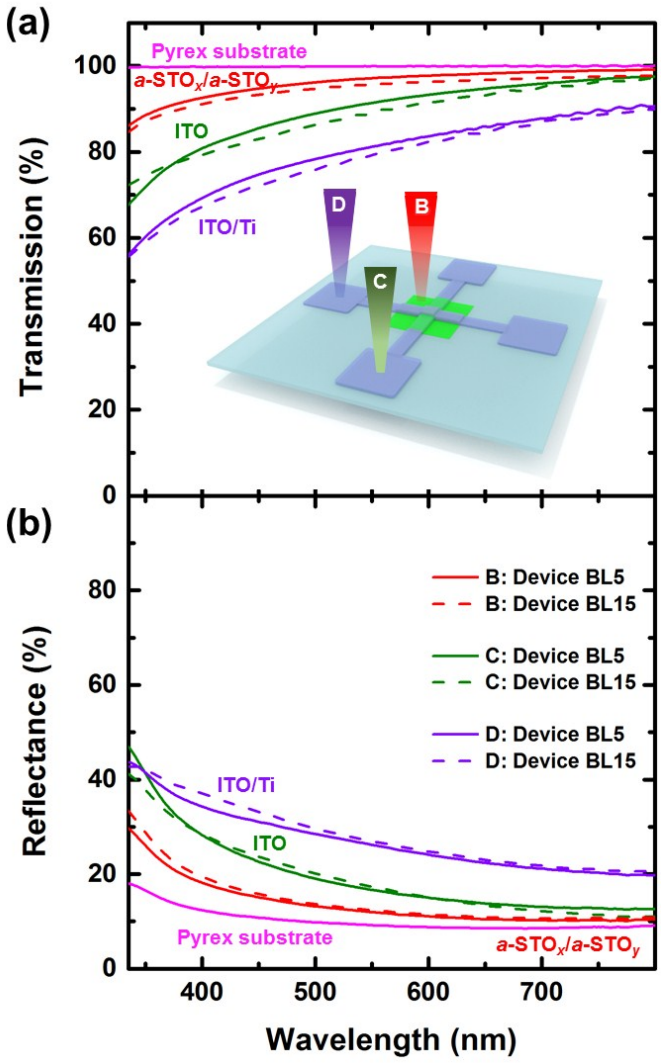

Fig. S5 Optical characteristics of the sputtered oxides. (a) UV-Vis transmission and (b) reflectance spectra of the bilayer *a*-STO_x/*a*-STO_y stack, bottom ITO and top ITO/Ti electrodes for Device BL5 and Device BL15. Inset shows a schematic of the regions on the cross-point cells used for the collection of transmission spectra for both devices and are highlighted by markers "B", "C" and "D" for bottom ITO electrode, *a*-STO_x/*a*-STO_y stack and top ITO/Ti electrode, respectively.

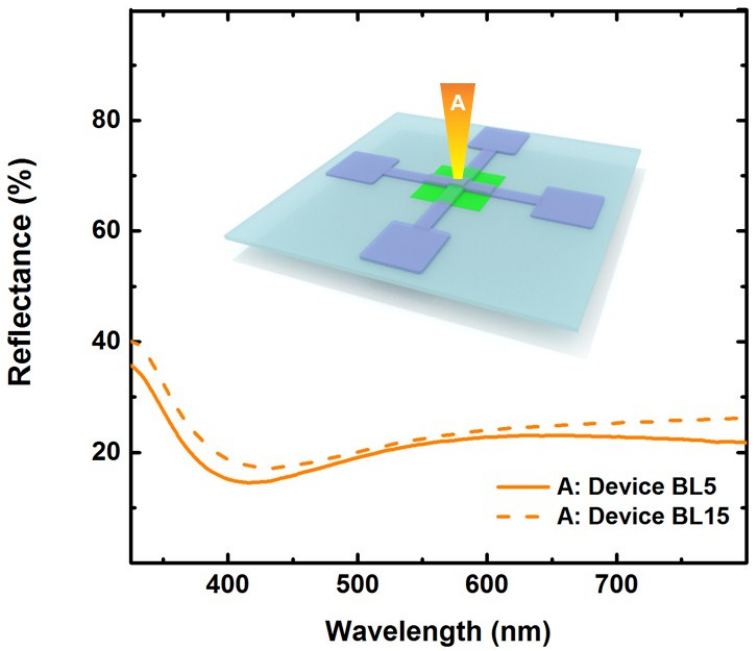

Fig. S6 UV-Vis reflectance spectra of Device BL5 and Device BL15 in 325-800 nm optical range. The spectra are collected from the device area highlighted by a marker "A" on the inset schematic of a cross-point device.

6. X-ray photoelectron spectroscopic (XPS) analysis of functional *a*-STO oxides

Fig. S7 shows the core-level binding energy spectra of oxygen (O 1*s*) and strontium (Sr 3*d*) in *a*-STO_x and *a*-STO_y oxides sputtered in a reducing (0% oxygen) and an oxidizing (5% oxygen) environment, respectively. In both oxides, O 1*s* spectra (Fig. S7a) can be fitted with two components with peak positions at 529.5 eV (±0.1 eV) and 531.3 eV (±0.1 eV), corresponding to O^{2-} ions in *a*-STO oxide[8] and C–O bond[8-10] formed due to adsorption of adventitious carbon onto the surface, respectively.

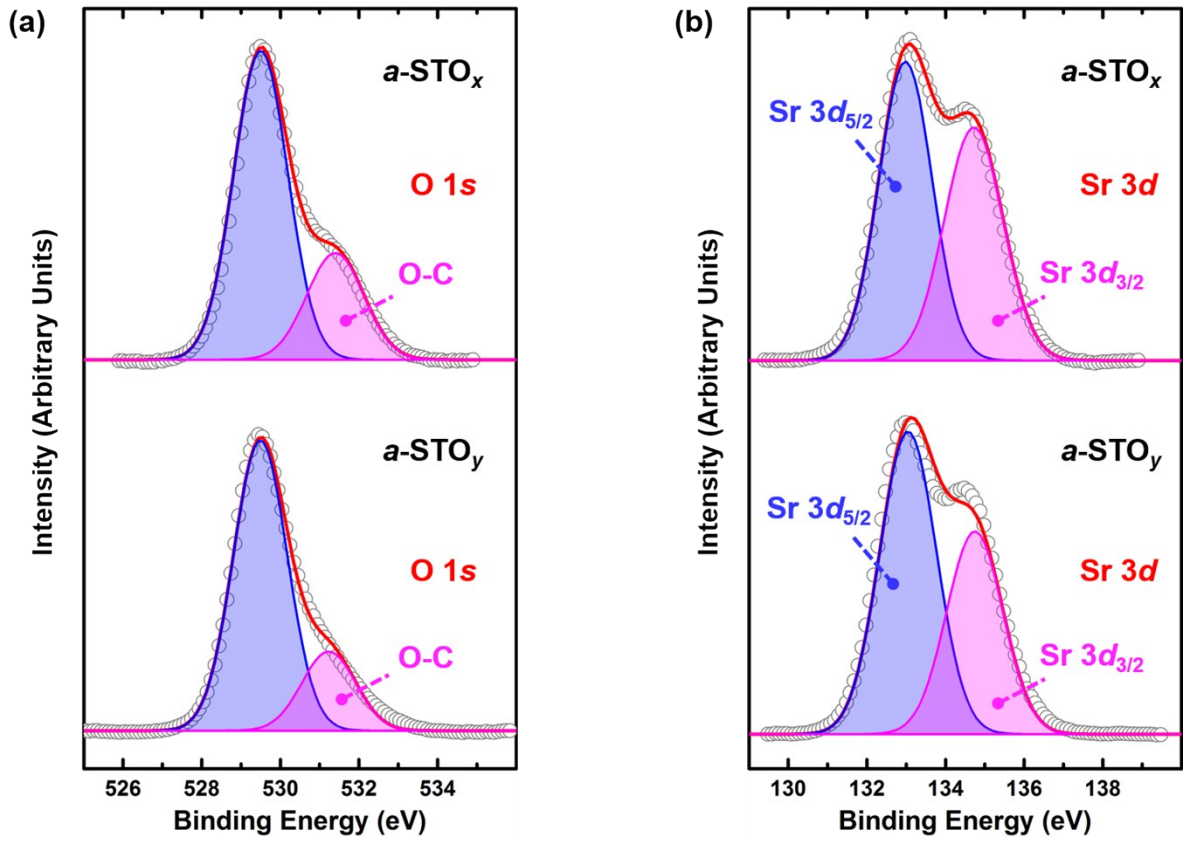

Fig. S7 Core-level XPS spectra of (a) O 1*s* and (b) Sr 3*d* for as-grown *a*-STO$_x$ and *a*-STO$_y$ oxides.

Furthermore, the core-level spectra of Sr 3*d* (Fig. S7b) could be fitted into a single component with no significient shift observed in chemical states. The binding energies for Sr 3$d_{5/2}$ at 132.9 eV (±0.1 eV) and for Sr 3$d_{3/2}$ at 134.7 eV (±0.1 eV) for both oxides, are attributed to Sr^{2+} species in *a*-STO.[8, 10]

7. Electroforming of *t*-ReRAMs

Fig. S8 shows the electroforming sweeps of 10×10 μm^2 *t*-ReRAMs while biasing from the bottom ITO electrodes. The Device BL15 (Fig. S8a) electroforms by applying -17.2 V and setting the current compliance at 100 μA. On the other hand, the Device BL5 (Fig. S8b)

electroforms by applying -14.5 V and the current compliance fixed at 5 µA. Comparatively higher electroforming current in the Device BL15 than the Device BL5 can be associated with the higher concentration of as-grown V_os in the Device BL15 owing to its thicker oxide stack. Under the influence of an electroforming voltage, the concentration of V_os further increases which results in the formation of conductive filamentary pathways and consequently an abrupt jump in current (limited by the current compliance at -100 µA) is observed at around -16.3 V (Fig. S8a).

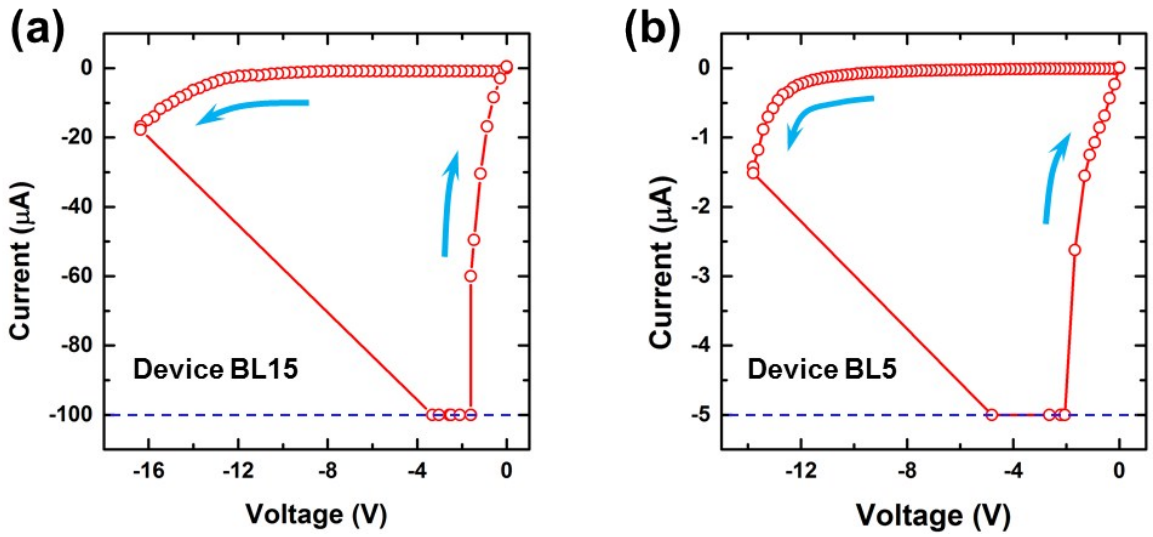

Fig. S8 The electroforming *I–V* sweeps of 10×10 µm^2 *t*-ReRAMs. The electroforming sweep of (a) Device BL15 where current compliance is fixed at 100 µA and (b) Device BL5 where current compliance is fixed at 5 µA.

8. X-ray diffraction spectra of ITO

The crystalline structure of as-deposited and post-deposition annealed ITO films (150 nm) on a glass substrate is investigated by X-ray diffraction (Bruker, D2 Phaser). In Fig. S9, the

diffractogram of annealed ITO (at 400 ˚C in ambient) shows a crystalline structure and can be indexed to cubic In_2O_3.[11, 12]

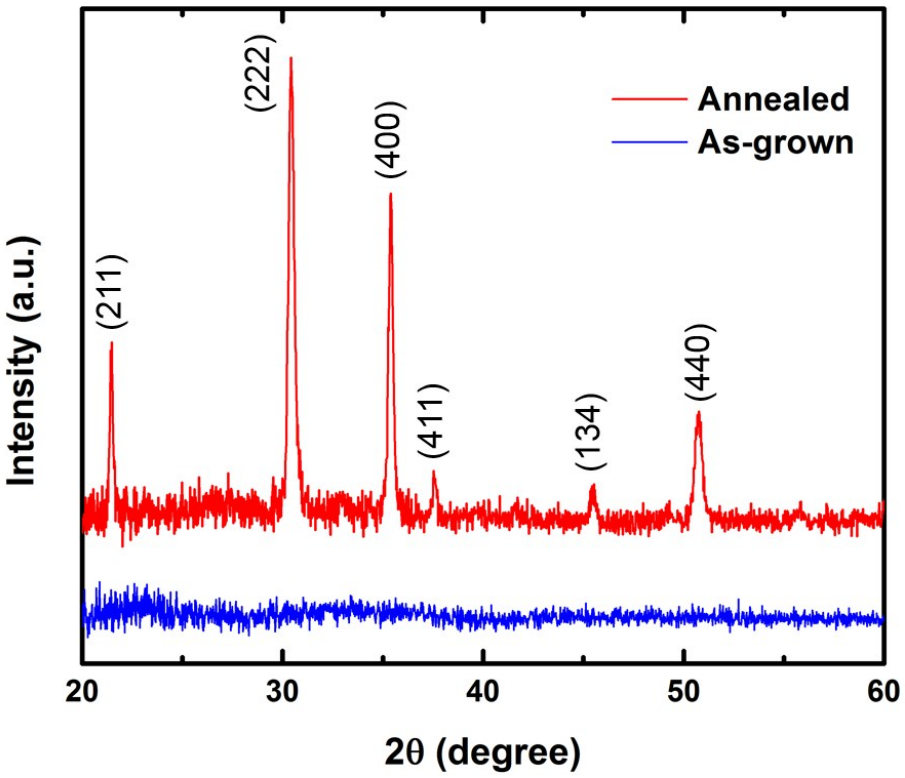

Fig. S9 X-ray diffractograms of room temperature sputtered and post-deposition annealed ITO thin films on pyrex substrates.

9. Electron energy loss spectroscopic analysis of *t*-ReRAM cells

Fig. S10 shows the titanium $L_{2,3}$ absorption edge of a virgin and an electroformed *t*-ReRAM cell. The fine structure from the electroformed cell is relatively more defined and the presence of t_{2g} peak indicates the higher morphological order in *a*-STO than the virgin cell.[13, 14]

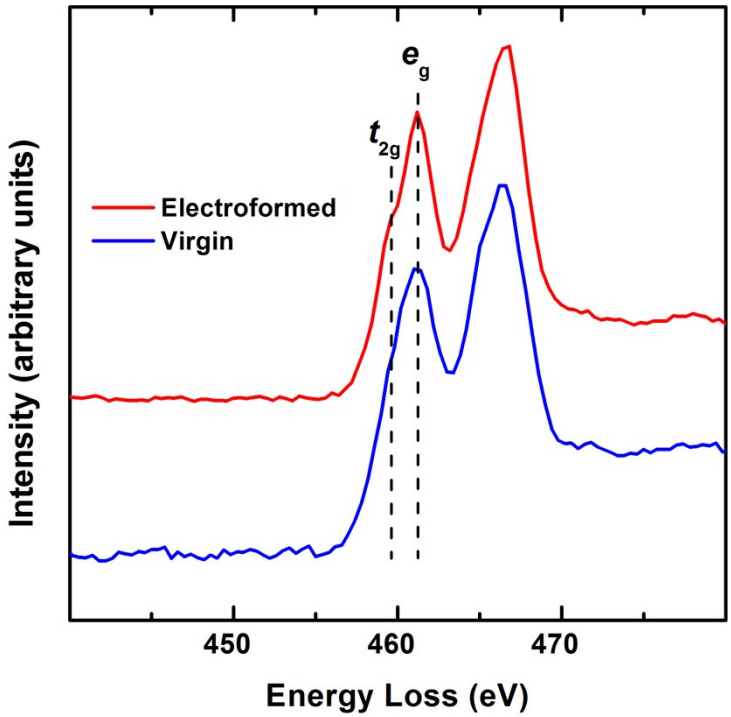

Fig. S10 Electron energy loss spectra of the virgin and electroformed *t*-ReRAM cells for the titanium $L_{2,3}$ edge.

10. Photoelectric characterization of *t*-ReRAM cells

The photoelectric response of *t*-ReRAM cells in HRS is measured under UV illumination (25±2 mW/cm^2) as a function of exposure frequency. Fig. S11 shows the photoelectric modulation in HRS of Device BL15 at 10 Hz of exposure frequency (Fig. S11a) and Device BL5 at 5 Hz (Fig. S11b) under read voltages of 0.25 V and 1 V, respectively.

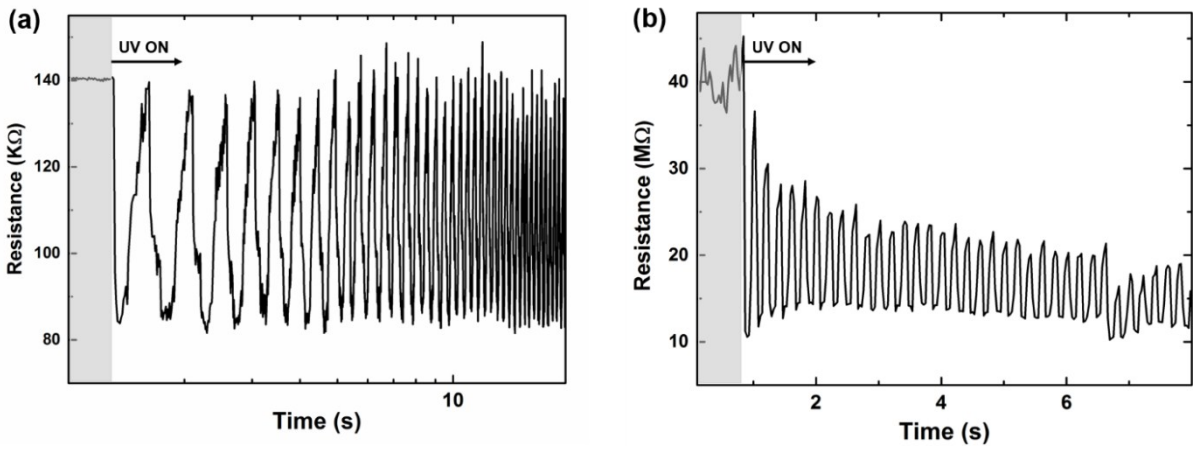

Fig. S11 Photoelectric modulation in HRS of the *t*-ReRAM devices. (a) Photoelectric response of Device BL15 at 10 Hz of exposure frequency, measured under a constant read bias of 250 mV. (b) Photoelectric response of Device BL5 at 5 Hz of exposure frequency, measured under a constant read bias of 1 V.

11. Photoelectric response of ITO electrodes

The optical response of top and bottom ITO electrodes to the different wavelengths (Fig. S12) shows that both electrodes are insensitive to the exciting illuminations.

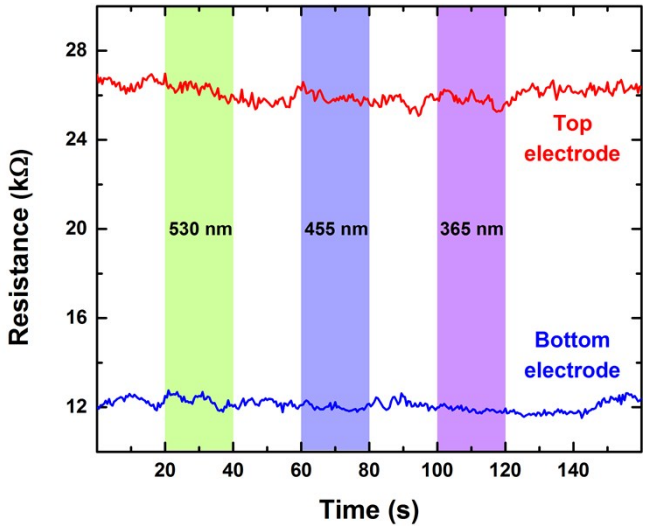

Fig. S12 The optical response of ITO electrodes to 365, 455, and 530 nm of illumination wavelengths at a V_{READ} of 100 mV.

References

1. R. Dittmann, R. Muenstermann, I. Krug, D. Park, T. Menke, J. Mayer, A. Besmehn, F. Kronast, C. M. Schneider and R. Waser, *Proc. IEEE*, 2012, **100**, 1979-1990.
2. R. Waser, R. Dittmann, G. Staikov and K. Szot, *Adv. Mater.*, 2009, **21**, 2632-2663.
3. M. Hansen, M. Ziegler, L. Kolberg, R. Soni, S. Dirkmann, T. Mussenbrock and H. Kohlstedt, *Sci. Rep.*, 2015, **5**, 13753.
4. J. H. Park, C. Buurma, S. Sivananthan, R. Kodama, W. Gao and T. A. Gessert, *App. Surf. Sci.*, 2014, **307**, 388-392.
5. A. Thøgersen, M. Rein, E. Monakhov, J. Mayandi and S. Diplas, *J. App. Phys.*, 2011, **109**, 113532.
6. L.-J. Meng, A. Maçarico and R. Martins, *Vacuum*, 1995, **46**, 673-680.
7. W. Wen-Fa, C. Bi-Shiou and H. Shu-Ta, *Semicond. Sci. Technol.* 1994, **9**, 1242.
8. D. Ehre, H. Cohen, V. Lyahovitskaya and I. Lubomirsky, *Phys. Rev. B*, 2008, **77**.
9. H. Nili, S. Walia, A. E. Kandjani, R. Ramanathan, P. Gutruf, T. Ahmed, S. Balendhran, V. Bansal, D. B. Strukov, O. Kavehei, M. Bhaskaran and S. Sriram, *Adv. Funct. Mater.*, 2015.
10. P. V. Nagarkar, P. C. Searson and F. D. Gealy, *J. Appl.Phys.*, 1991, **69**, 459.
11. Y.-F. Lan, Y.-H. Chen, J.-L. He and J.-T. Chang, *Vacuum*, 2014, **107**, 56-61.
12. T. O. L. Sunde, E. Garskaite, B. Otter, H. E. Fossheim, R. Sæterli, R. Holmestad, M.-A. Einarsrud and T. Grande, *J. Mater. Chem.*, 2012, **22**, 15740.
13. R. F. Egerton, *Electron Energy-Loss Spectroscopy in the Electron Microscope*, Springer, US, 3 edn., 2011.
14. J. Rho, J. Kim, S. Shin, J. Kwon, M. Kim, J. Song and E. Choi, *J. Lumin.*, 2010, **130**, 1784-1786.